Experimental study on WFeNiMo high-entropy alloy projectile penetrating semi-infinite steel target

Hai-hua Chen [a], Xian-feng Zhang [a, *], Lan-hong Dai [b, c], Chuang Liu [a], Wei Xiong [a], Meng-ting Tan [a]

[a] School of Mechanical Engineering, Nanjing University of Science & Technology, Nanjing, Xiaolingwei 200, Jiangsu, 210094, China
[b] State Key Laboratory of Nonlinear Mechanics, Institute of Mechanics, Chinese Academy of Sciences, Beijing, 100190, China
[c] School of Engineering Science, University of Chinese Academy of Sciences, Beijing, 101408, China

ARTICLE INFO

ABSTRACT

The appearance of high-entropy alloys (HEAs) makes it possible for a material to possess both high strength and high ductility. It is with great potential to apply HEAs under extreme conditions such as in the penetration process. In this paper, experiments of WFeNiMo HEA and tungsten heavy alloy (WHA) projectiles penetrating medium-carbon steel were conducted by using the ballistic gun and two-stage light-gas gun that can accelerate projectiles to impact velocities ranging from 1162 m/s to 2130 m/s. Depth of penetration (DOP) at elevated impact velocities of HEA and WHA projectiles were obtained firstly. Combined with the macroscopic and microscopic analysis of the residual projectiles, the transition of the penetration mode of the WFeNiMo HEA projectile was identified systemically. The experimental results indicated that the penetration mode of the HEA projectile changes from self-sharpening to mushrooming with the increase of impact velocity, while for the WHA projectile, the penetration mode is always mushrooming. The microstructure of the residual HEA projectiles showed that the phases tangle with each other and the morphology of the microstructure of the phases differs in the two penetration modes. Besides, the evolution of shear bands and fractures varies in the two modes. The evolution of the microstructure of HEAs causes the sharp-pointed nose to disappear and the HEA projectile ultimately becomes blunt as the impact velocity increases.

1. Introduction

High-entropy alloys (HEAs) have broken the traditional alloy design approach confined to single or binary alloys because of their properties. HEAs contain at least four major alloying elements in either equi-molar or near equi-molar ratios and exhibit excellent mechanical properties, especially high strength in comparison to conventional alloys and have garnered considerable research interest [1–4]. Unique characteristics of HEAs can be expressed as four core effects, high-entropy effect, lattice distortion effect, sluggish diffusion effect and cocktail effect [5–7]. The high-entropy effect makes the high-entropy phases stabilize, such as the solid-solution phases. Since the size of different elements can be very different in some cases, this can lead to severe lattice distortion, which in turn is also used to explain the high strength of HEAs. The sluggish diffusion effect can explain the formation of nano-sized precipitations because the nuclei form easily but grow slowly. For HEAs, each element has the same possibility to occupy a lattice site if chemical ordering is ignored. For metallic alloys, this effect indicates that the unexpected properties can be obtained after mixing many elements, which cannot be obtained from any one independent element. The sluggish diffusion provides a method for the projectile to balance strength and toughness. The lattice distortion improves the strength of the alloy and the high strength raises the penetration ability. The four core effects of HEAs show the diversity of application prospects and its control of strength and plasticity may facilitate the development of potential materials with excellent mechanical properties under extreme conditions.

Recently, scholars have devoted themselves to the research of new materials which exhibit self-sharpening behavior in

* Corresponding author.
  E-mail address: lynx@njust.edu.cn (X.-f. Zhang).
  Peer review under responsibility of China Ordnance Society

penetration, especially by using the amorphous alloy composite projectile. Martin et al. [8] carried out impact experiments on zirconium-based metallic glass rods by performing a reverse ballistic test and it was found that the shear fracture angle was about 42.5°. Conner et al. [9] conducted experiments of the 85% W-wire reinforced metallic glass projectile impacting aluminum and steel targets. The penetration depth of the metallic glass composite projectile increased by 10−20% compared to WHA at the same velocity. It was showed that the initial cylindrical projectile nose took on a conic shape after penetration. In Choi-Yim's research [10], the tests of the 50% W/R particulate reinforced metallic glass projectile penetrating into aluminum and steel targets were performed and obtained results similar to Conner's. Chen et al. [11−14] studied the penetration behavior of the tungsten fiber reinforced metallic glass composite projectile by performing the armor piercing test. It was found that the projectile could not penetrate the target effectively until it reached a high velocity about 800 m/s and showed self-sharpening. From related literature, it can be concluded that most of the projectiles with self-sharpening behavior are mainly made form amorphous composite materials. Most researches concentrate on the experiment results such as depth of penetration, while the self-sharpening mechanism and penetration behavior at high impact velocities of the new materials are still to be investigated.

In addition, it is necessary to develop theoretical models to characterize the hydrodynamic penetration behavior. Tate [15,16] and Alekseevskii [17] proposed a modified Bernoulli equation to describe the one dimensional penetration behavior and used the classic Tate-Alekseevskii model [18]. Rosenberg et al. [19] improved the Tate-Alekseevskii model by introducing the equivalent cross-sectional area due to the non-uniformity of the force acting on the mushroom head from the center to the edge of the projectile in the penetration process. Sun et al. [20] proposed a modified target resistance by taking the difference between the cross-sectional area and the crater area into account. Zhang et al. [21] modified the A-T model based on the nose shape of the projectile in the penetration process. The Bernoulli equation describing the relationship between resistance and penetration velocity was modified by Anderson et al. [22] through simulations. The united model for metallic and concrete targets was proposed by Kong et al. [23] based on the cavity expansion theory. The influencing factors includes the nose shape [24], the length to diameter ratio [25,26] and the dynamic resistance stress [25,27]. These parameters affects self-sharpening and need to be explored further.

The research on mechanical behavior of HEAs is mainly focused on quasi-static compression and tension [28−31]. A relatively small amount of compressive deformation behaviors under high strain rates has been investigated [32−36]. Zhang et al. [37] conducted a ballistic research in HEAs bullet penetrating steel plates and the HfZrTiTa$_{0.53}$ HEA showed a large amount of heat release upon high-speed impact and good penetration performance. Liu et al. [38] developed a new chemical-disordered multi-phase tungsten high-entropy alloy that exhibits outstanding self-sharpening capability and leads to a 10−20% better penetration performance than conventional tungsten heavy alloys. Almost no research has been made in the penetration behavior of HEA projectiles when the impact velocity reaches a higher value. The penetration behavior of HEA projectiles with a wide impact velocity range is also worth investigating, which will shed more light on the properties of HEAs and promote its application in ammunition.

In this paper, a comparison experiment on WFeNiMo HEA and WHA (93W-4.9Ni-2.1Fe, wt.%) projectiles penetrating into medium carbon steel targets were carried out. Both DOP and residual projectiles were obtained and analyzed after the experiments. The residual projectiles were investigated from both the macrostructure and microstructure for the further study of the penetration mode transition of HEA and WHA projectiles. The experimental results gave the properties of HEAs at high strain rates and high temperatures, which will help promote the HEA composition design.

2. Experiments of HEA and WHA projectiles penetrating into steel targets

2.1. Fabrication of WFeNiMo HEA

Tungsten heavy alloys possessing high density and excellent mechanical properties are widely used in the penetration field. The element type of the WFeNiMo high-entropy alloy is similar to that of the tungsten heavy alloy (W, Fe, and Ni). Mo is an element in the same family as tungsten. The content of each element is different in the two alloys. The chemical compositions of the HEA and WHA are list in Table 1. The WFeNiMo HEA was prepared by the electro-magnetic levitation melting technology in a water-cooled copper crucible from raw materials with a purity of 99.9% in an inert atmosphere. To achieve a homogeneous distribution of constituent elements, the as-prepared alloy was re-melted four times and then kept in the liquid state for 20 min each time. The density of the HEA was about 12.7 g/cm^3, and that of the WHA was 17.7 g/cm^3. For more details of the HEA fabrication, readers can refer to our previous paper [38]. Fig. 1(a) shows the HEA specimen and in Fig. 1(b) are the HEA projectiles with a length of 50 mm and a diameter of 7 mm.

2.2. Experimental scheme and layout

The WHA and HEA projectiles have the same shape, namely, 7 mm in diameter and 50 mm in length. The target was medium-carbon steel of cylindrical shape with a diameter of 200 mm and a thickness of 150 mm. To eliminate the influence of boundary effect, the diameter of the target was set about 30 times of the projectile diameter.

In order to achieve higher impact velocities, a sub-caliber launching technique was employed in the penetration experiment. As shown in Fig. 2 the aluminum sabot, made of hard aluminum and cut into three pieces along the circumferential direction evenly, was designed to seal propellant gas. An aluminum bottom pusher was used to connect the sabot and nylon ring and also support the sabot propelling in the gun. The nylon ring can seal the high pressure gas behind the projectile and improve the energy utilization of the gunpowder during the acceleration of projectile. Similarly, a resin sabot was designed for the two-stage light-gas gun.

The experiment layout is shown in Fig. 3. Projectiles were fired from a ballistic gun at lower impact velocities and from a two-stage gas gun to achieve higher impact velocities (>1700 m/s). A total of two velocity screens for velocity measurement were placed 1 m apart behind the sabot collector. A time recorder was started as the projectile arrived at the first velocity screen and stopped when arriving at the second one. Then the projectile's velocity could be calculated. A medium-carbon steel target was placed behind the second velocity screen. The projectile's flying attitude and the

Table 1
Composition of the two materials.

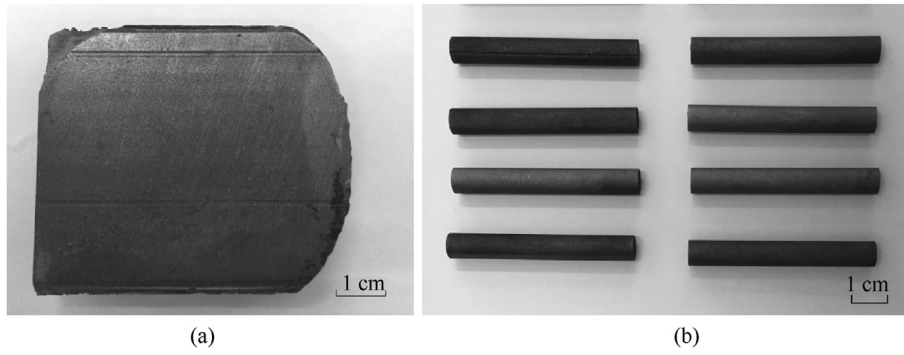| Material	W	Fe	Ni	Mo
HEA/%	27.5	24.4	23.5	24.6
WHA/%	85.5	4.7	9.8	/

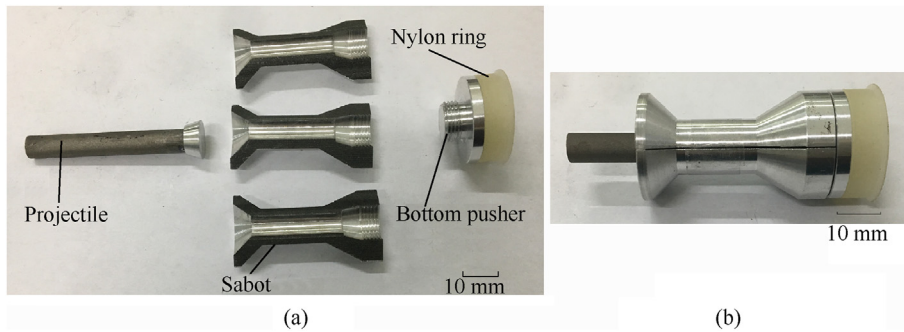**Fig. 1.** WFeNiMo high-entropy alloy (a) Specimen; (b) Projectiles.

Fig. 2. Sabot projectile (a) Components; (b) Projectile in entirety.
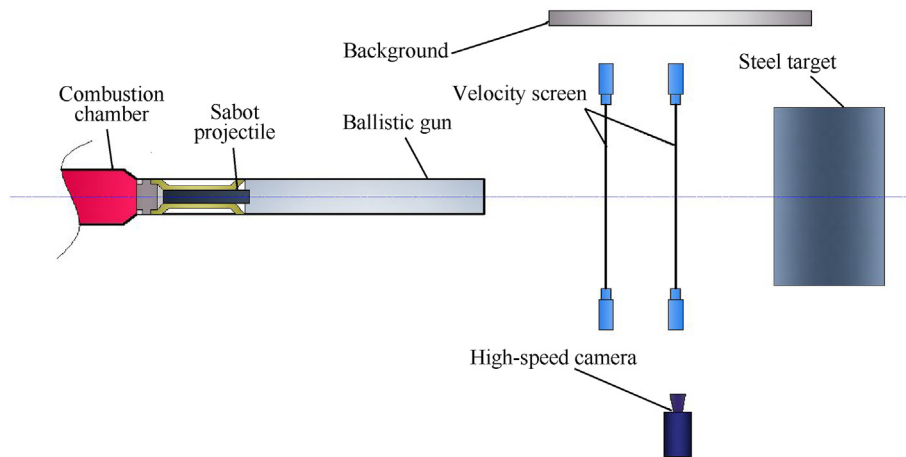

Fig. 3. Layout of impact experiment setup.

collision between the target and the projectile were recorded by the high-speed camera. The frame rate of the camera was 12000 fps. As shown in Fig. 4, the projectile's flying attitude was stable and the attack angle was almost 0° when the projectile hit the target. Thus it can be regarded as a normal impact. From the photo recorded by the high-speed camera in Fig. 5(a), the material of projectile and target forms bowl-shaped backward jets during impact. The kinetic energy of the projectile was converted to plastic energy and thermal energy, and the projectile nose rapidly entered the quasi-fluid state of uniform deformation in the transient high-pressure stage. In Fig. 5(b), the contact between the projectile and the target blazed without stable reflux, from which it can be inferred that the impact between HEA and the steel target causes energy release effect.

3. Ballistic performance of WHA and HEA projectiles

26 shots were analyzed totally in this research. 16 shots were conducted in the previous study [38] and 10 shots at high impact velocities were added in this study to investigate the high-velocity penetration behavior. 10 penetration experiments of the projectile impacting the medium-carbon steel target were carried out, with 6 shots for WHA projectiles and 4 for HEA projectiles. The impact velocity varied from 1162 m/s to 1700 m/s for WHA projectiles and from 1531 m/s to 2130 m/s for HEA projectiles.
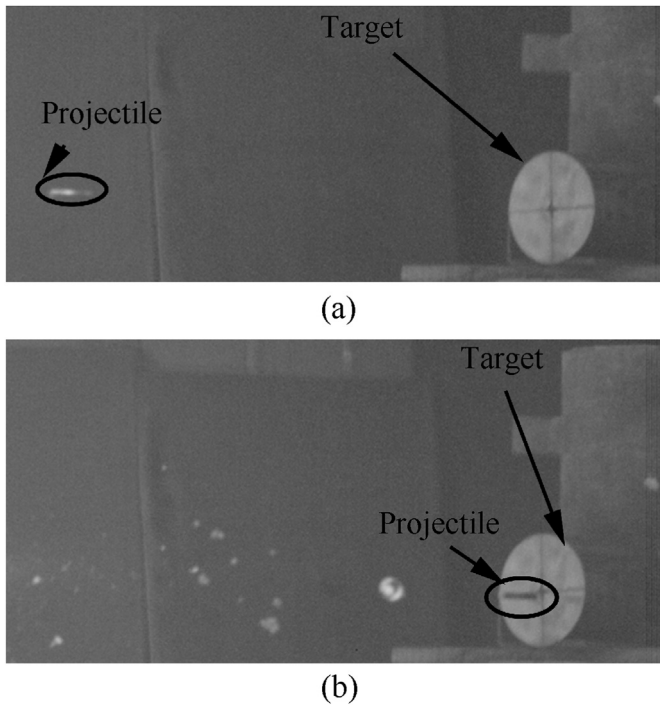
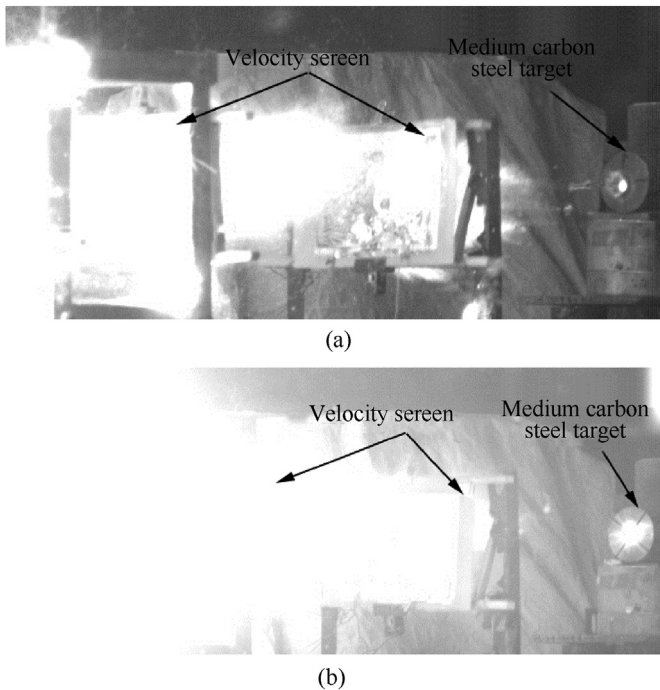**Fig. 4.** Projectile's flying attitude: (a) Projectile flying in the air; (b) Projectile approaching the target.

Fig. 5. Moment of the projectile hitting the target: (a) WHA projectile; (b) HEA projectile.

3.1. Variation of penetration channels under different impact velocities

A number of important differences between HEA and WHA projectiles were figured out from the penetration experiment results. In order to investigate more experiment details, it is necessary to cut through the metal targets by wire-electrode cutting. Profiles of medium-carbon steel targets impacted and penetrated by WHA and HEA projectiles are presented in Fig. 6 and Fig. 7 respectively. The variation in penetration channels under different impact velocities is analyzed as follows. The penetration channel is obvious when the impact velocity of WHA projectiles starts from 917 m/s. The residual material is embedded in the steel target, forming a typical shape of mushroom head. The penetration channel is relatively straight and smooth with no obvious change in radius. Differently from WHA projectiles, the penetration effect of HEA projectiles on medium carbon steel targets can hardly be observed when the impact velocity is lower than 900 m/s. Only a shallow hemispherical crater is formed on the target surface at the impact velocity of 876 m/s. Although there is no obvious penetration channel when the velocity is 915 m/s, the penetration depth increases to 12 mm. The penetration channel does not appear until the velocity reaches 980 m/s. It can be seen that irregular fish-scales distribute on the channel surface and the crater radius on target surface is larger than that of WHA projectiles. When the impact velocity is greater than 1087 m/s, the whole penetration channel appears to be a cone, which reflects that the interaction area between the projectile nose and the target decreases continuously in the penetration process. When the impact velocity continues to increase, the taper of the channel becomes smaller, indicating that the nose of projectile becomes sharp in the penetration process. When the impact velocity reaches 1779 m/s, the penetration channel becomes straight and the projectile blunt, indicating that the penetration mode has changed.

3.2. DOP and VOPC (volume of penetration channel) at elevated impact velocities

The penetration data of the 26 projectiles are included in Table 2. It is more appropriate to characterize the impact conditions by kinetic energy per volume ($1/2\rho v^2$) because of the density difference between the two materials. The *KE* (Kinetic energy per volume)-DOP diagram is shown in Fig. 8(a). Combined with the transformation of the projectile nose and penetration channel in Fig. 7, it is obvious that the penetration mode of WFeNiMo HEA changes at velocities between 1330 m/s and 1531 m/s. It is defined that the at lower impact velocities is the self-sharpening penetration mode (<1330 m/s) and at higher velocities is the mushrooming penetration mode ($\geq$1531 m/s). When the HEA projectile enters the self-sharpening penetration mode, the cross sectional areas of the nose are smaller than that of the nose in the mushrooming penetration mode. The penetration resistance of the self-sharpening penetration mode is smaller than that of the mushrooming penetration mode. When the HEA projectile enters the mushrooming penetration mode, the mushroom head increases the penetration resistance and reduces the penetration ability, thereby increasing the diameter of the bullet hole and decreasing the DOP. The rate of DOP growth decreases with the increase of impact velocity. The DOP of WFeNiMo HEA projectiles increases sharply and is deeper than that of WHA projectiles in the self-sharpening penetration mode. The penetration ability of the HEA projectile does not become weaker than that of the WHA projectile until the *KE* reached to 16 kJ/cm^3 (the corresponding impact velocity is about 1650 m/s). However, the DOP of the WHA projectile exceeds that of the HEA in the fluid penetration mode with the enhancement of the impact velocity.

The *KE*-VOPC in Fig. 8(b) shows the distinct superiority of the HEA in excavating. The VOPC of the HEA increases by 18% compared with the WHA under high *KE* (25 kJ/cm^3). When the WHA projectile penetrated into steel target, the material separated from the nose had less contact with the target due to its strong plastic
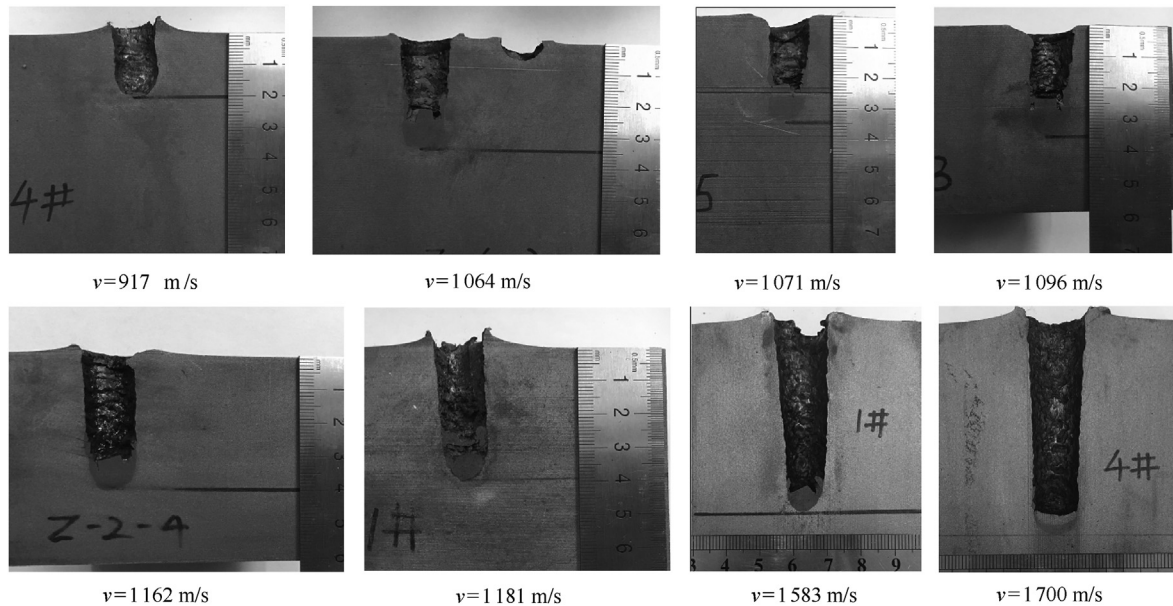
v=917 m/s	v=1 064 m/s
v=1 071 m/s	v=1 096 m/s
v=1 162 m/s	v=1 181 m/s
v=1 583 m/s	v=1 700 m/s

Fig. 6. Target profile of WHA projectiles.

deformation ability. When the HEA projectile penetrated into steel target, material separated from the nose and flowed out of the crater similarly. The separated material had more interaction with the target due to its certain brittleness. The severe friction and cutting of separated material promoted the cratering of the target. Besides, there are a large amount of Ni elements in the HEA. The element is active and reacts easily with oxygen in the air. The reaction released some chemical energy when the projectile penetrated into the target and the energy increased the VOPC.

3.3. Shape of residual projectile under different impact velocities

From the photos of post-test targets in Fig. 9, the radius of the penetration channel of the WHA projectile changes inconspicuously while the channel of the HEA projectile shows an obvious taper. Furthermore, the surface of the WHA projectile penetration channel shows a smooth wavy flow, suggesting that the material of the projectile nose continuously flew out from both sides and spreads evenly in the target. The residual WHA projectile, found at the bottom of the penetration channel, is approximately hemispherical and the diameter is about two times larger than that of the original state. It demonstrates that the deformation of the projectile nose produced plastic flow and the contact between the projectile and the target was tight. The material was extruded and then flew to the tail of the projectile, which shows its excellent plastic deformation ability. The mushroom head forms in the projectile nose ultimately.

Compared to the penetration channel of the WHA projectile, there are many irregular small protrusions on the surface of the HEA projectile penetration channel, reflecting a different penetration status. It is inferred that the internal structure of HEAs is composed of two phases at least rather than simply a single phase. From the residual nose of the HEA projectile, the nose is sheared at an angle of about 45° to the axis of the projectile without obvious plastic deformation. The projectile nose is tapering and the maximum diameter of the part is approximately equal to that of the original state. The projectile material shows little plasticity after being extruded from the nose and is radially distributed along the surface of the penetration channel. It can be inferred that the HEA

has insufficient plastic deformation ability or intermittent plastic flow in the penetration process. There is a clear gap and few residual material stagnations between the HEA residual projectile and the target. The material on both sides of the projectile nose were separated from the projectile body and flew out quickly. As a result, the nose became sharper in the penetration process.

During the WHA projectile penetration, the material transformed from semi-fluid state to fluid state as the impact velocity increases, but the shape and radius of the penetration channel exhibit little variation as is shown in Fig. 10(a). However, during the WFeNiMo HEA projectile penetration, the material self-sharpened first and then became fluid and the shape of the penetration channel under low impact velocities was tapered which is different from the straight channel under high impact velocities from Fig. 10(b). An inflection point of the HEA penetration mode exists according to the channel shape.

The results show that the penetration behavior of the HEA projectile differs from that of the WHA projectile in many aspects, such as the penetration channel shape, the residual projectile nose shape and the inflection point of the HEA projectile. Some conclusions are as follows:

(1) The HEA projectile nose sharpens continuously in the self-sharpening penetration mode and becomes blunted in the mushrooming penetration mode. Mushroom head formed in the WHA projectile penetration process.
(2) The HEA projectile cannot enter the self-sharpening penetration mode until the velocity or the KE reaches a certain threshold.
(3) The HEA projectile has more superior ability in excavating than the WHA projectile under the same KE, while the result is contrary when they are at the same velocity.

In summary, the physical mechanism of the interesting phenomenon, especially the self-sharpening behavior, cannot be revealed on the macroscopic scale. It is necessary to analyze the microscopic state of the HEA to investigate the mechanism at a deeper level.
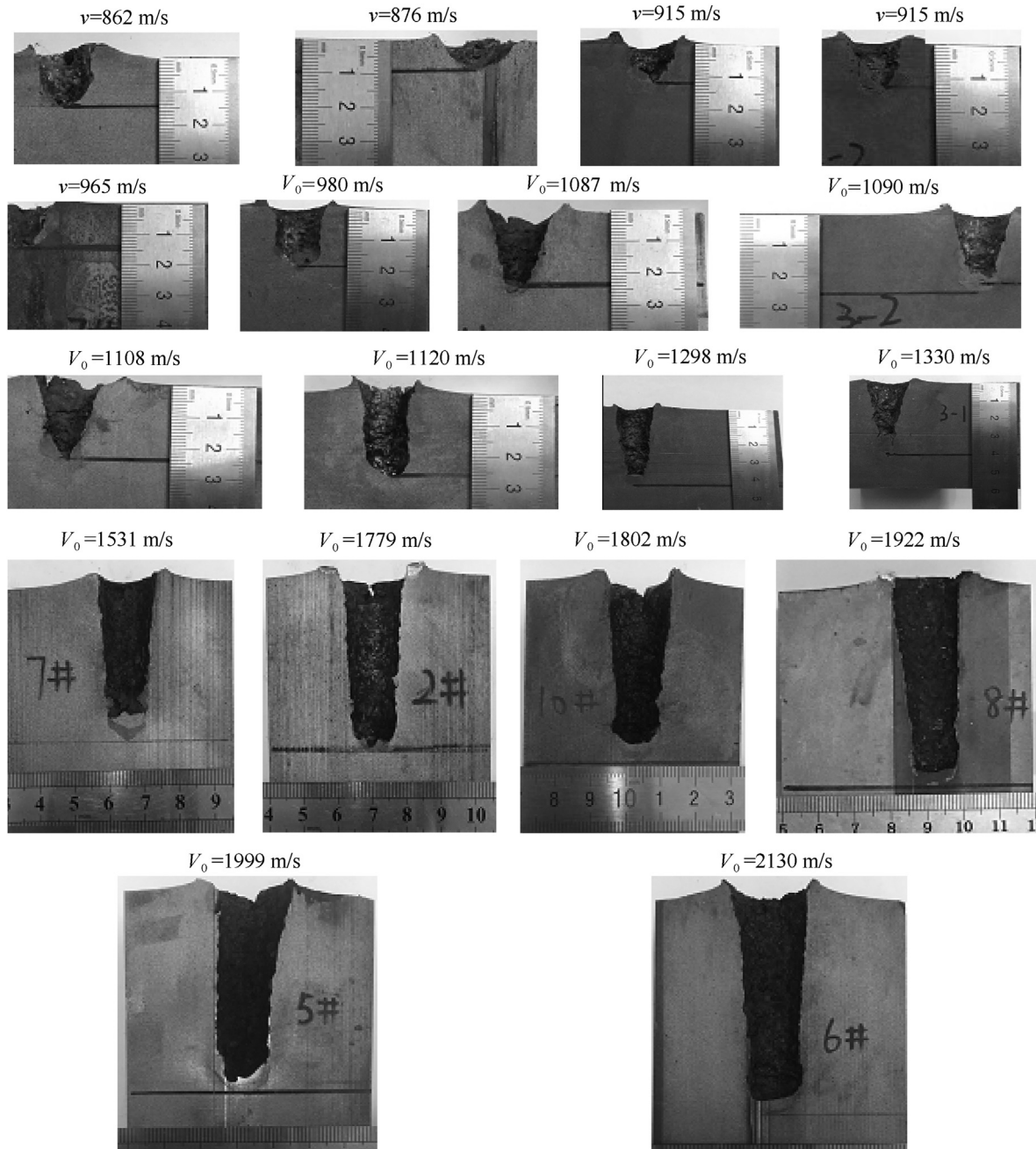
Fig. 7. Target profile of HEA projectiles.

4. Microscopic analysis of residual projectiles under different impact velocities

4.1. WHA projectiles in mushrooming penetration mode

In the case of high-speed penetration, the nose of the projectile undergoes a series of deformation such as extrusion, cracking, abrasion, and melting, which also includes loss of masses and changes in the shape of the projectile nose. Fig. 11 shows the metallography of the mushroomed nose of a WHA projectile under the impact velocity of 1096 m/s.

It is observed that there are two obvious cracks in the residual projectile nose: one is a circular arc crack at the bottom of the penetration channel and the other is a wide crack intersecting with the circular arc crack.

Six regions a, b, c, d, e and f are marked on the residual projectile of the WHA in Fig. 11. In contrast to the metallographic structure of the rigid body of the WHA (region-a), it can be observed that the grains in the front of the mushroom head (region-d) are subjected to axial compression and appear squashed. The grains in the region-c and region-e near the contact surface are approximately flattened and elongated along the tangential direction of the contact face. The gap between grains is also compressed. With the grains moving away from the contact face, the direction of grain elongation is different from that near the contact surface. The turning angle of the grain and the amount of deformation decrease when the position is closer to the axis of the nose. The region-b is the intersection of the arc crack and the wide crack, where the

Table 2
Penetration test results of WHA and HEA LRP.

Projectile material	Impact velocity/(m·s⁻¹)	Projectile mass/g	Kinetic energy/kJ	DOP /mm	VOPC /mm³
WHA	917	33.30	7.28	20	2944
	1064	33.30	9.80	34	4882
	1071	33.30	9.93	34	4175
	1096	33.30	10.40	36	4963
	1162	33.30	11.69	40	6118
	1181	33.30	12.07	39	6796
	1583	33.30	21.69	57	9449
	1700	33.30	25.00	66	12216
WFeNiMo HEA	862	22.02	4.25	14	1821
	876	21.03	4.20	9	1844
	915	21.72	4.73	12	2333
	915	23.12	5.03	13	1956
	965	23.06	5.58	14	2719
	980	21.95	5.48	18	3389
	1087	22.29	6.85	23	3922
	1090	22.30	6.89	22	4067
	1108	24.17	7.71	25	4067
	1120	24.02	7.83	26	4000
	1298	22.03	9.65	42	6886
	1330	22.62	10.40	40	8936
	1531	23.95	14.60	45	6486
	1779	21.66	17.82	49	10257
	1802	22.66	19.12	52	10538
	1922	22.53	21.64	57	10647
	1999	21.54	22.38	55	12234
	2130	21.70	25.60	63	15247

elongation direction of the grain is nearly parallel to the extension direction of the large crack. The closer the grain is to the crack surface, the greater its deformation degree is. In general, the deformation degree of the grain is consistent with the macroscopic deformation degree of the projectile, which means the pressure on the projectile nose decreases from the contact surface to the inside and the pressure on the projectile nose is gradient.

As the impact velocity increases, a deflection against the penetration channel appears and less WHA residual projectile remains than at low impact velocities. From the metallography of the WHA residual projectile near the interface in Fig. 12, the material is compressed tightly and there is almost no gap among grains, indicating that the projectile deforms more sharply than at low impact velocities compared to Fig. 11.

4.2. Transition from self-sharpening to mushrooming penetration of HEA projectiles

4.2.1. Self-sharpening penetration mode at lower impact velocity

The metallographic diagram of the HEA residual projectile (v = 1330 m/s) is shown in Fig. 13. At least two randomly distributed phases have relatively similar contents. The phases showed more complex mobility behavior in the penetration process, which is different from conventional alloys dominated by a single element. On the basis of micro analysis, the WFeNiMo HEA has three phases, i.e., BCC, FCC and μ phases [38]. The μ phase has an extremely small proportion of the alloy and is neglected in the following analysis. The darker part is the soft phase and the lighter part is the hard one in the HEA [38]. The distribution of the two phases presents the morphology of the soft phase wrapping the discontinuous hard phase in most cases while the hard phase seldom wraps the relatively soft phase.

Region-a is the tip of the projectile nose, where the morphology of the hard phase is different from that in the original state (region-g). The phase distribution is relatively scattered and there is a large area of continuation in the original state. The hard phase accounts for a significant increase in region-a and the alloy presents a small granular adhesion phenomenon where the hard phase wrapping the soft phase occurs. The hard phase also exhibits significant agglomeration and gets elongated along the crack propagation in region-b and region-c. It can be seen that the material near the contact interface tends to flow against the penetration velocity direction in region-d. The hard phase is elongated along the flow direction and aggregates at the fracture position, which is consistent with the observation at region-e. In region-f, a fracture exists across the whole projectile, which cannot be observed on the macro level.

The self-sharpening penetration is one of the focuses in the field of armor piercing. Tungsten heavy alloy (WHA) and depleted uranium (DU) are two main materials for armor piercing projectiles. Due to WHA's lower ductility and higher modulus, the tungsten penetration tends to break into pieces in the nose area or along its length. If the ductility of the rod is increased, the result will be an inefficient penetrator due to mushrooming of the nose and/or severe bending [39]. Conversely, the DU rod tends to "ablate" as it passes through armor. Its nose is worn away in relatively fine pieces while a reasonably efficient front cross section is constantly presented to the remainder of the target. This behavior is primarily attributed to the high strength and low elastic modulus (e.g. sound speed) inherent in DU penetration [39]. For two other families of uranium alloys (U-3/4Ti and the U−8Mo), localizations quickly develop in the plastic flow. resulting in a rapid discard of the deformed material from the head of the penetrator [40]. The self-sharpening penetration mechanism of the HEA is different from that of the DU. Studies [38] showed that the multi-phase structure of the HEA promotes the inhomogeneous deformation and causes a large strain gradient between the precipitations and the fcc matrix. The stored energy, manifested as high-density dislocations associated with the strain gradient, drives dynamic recrystallization softening that contributes to the formation of shear bands and the resultant self-sharpening behavior. However, more details about the self-sharpening behavior should be explained. From the
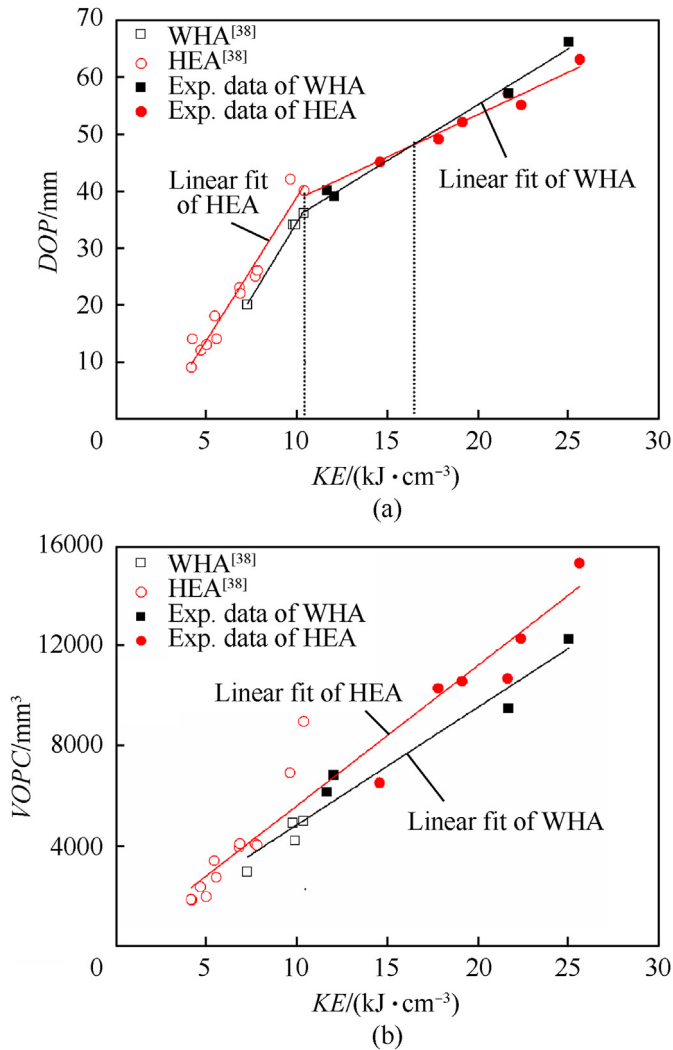
(a)

(b)

Fig. 8. Experiment results (a) $KE(1/2\rho v^2)$-DOP; (b) $KE(1/2\rho v^2)$-VOPC.

residual projectile in Fig. 14, three residual projectiles with different shapes are shown, indicating the complexity of the HEA penetration process. When the HEA projectile entered into the steel target, it changed from a cylindrical bar to a rod with a blunt nose in stage I. The transition indicated the finite plasticity of the HEA and the deformation in the nose is inhomogeneous. With the aggravation of deformation, the shear bands developed and some material was separated from the nose in stage II. The evolution of the shear bands originated in the multi-phase structure. From the stage III, the sharp nose shape was converted to an almost flat one, the same with the initial nose shape of the HEA projectile.

The self-sharpening penetration can be divided into three stages which form a cycle in the self-sharpening penetration process. Some evidence for the microstructure of the residual HEA projectile suggests the evolution of the self-sharpening penetration in Fig. 15. From mode I to mode II, the shear band was observed in the projectile nose, and the crack developed near the shear band which caused the material to be separated from the nose. From mode II to mode III, a subtle crack developed between the nose and the cylindrical part due to the wave propagation and the direction of the crack was perpendicular to the penetration velocity. The crack appeared in the fcc phase in most cases as the strength of the fcc phase in the HEA is lower than the bcc phase. More details about the crack are shown in Fig. 16. On both sides of the crack, phases show finite plasticity compared with the phases suffering intense compression near the shear band. The crack is taken as typical brittle fracture features. It is similar to Li's research [41] where the fcc phase which was regarded as the weak phase started to deform and the bcc phase which was considered as the hard phase deformed later when the alloy suffered larger pressure. As is known to all, the compression and tensile wave propagation in the projectile is very complex, and the projectile will break into several parts if it cannot endure the wave propagation.

4.2.2. Mushrooming penetration mode at higher impact velocity

The mushrooming penetration mode is defined in view of the different penetration channels formed by the HEA projectile in Fig. 7 and the transition of penetration efficiency in Fig. 8(a). When the HEA projectile penetrates the target at a higher velocity ($v = 1999$ m/s), no integrated nose remain as shown in Fig. 17. From the residue of the projectile, the two phases produce marvelous change where phases of the HEA become disordered in shape and appearance. The proportion of the hard phase decreases sharply compared with that in the self-sharpening penetration mode.

The microstructure of the HEA in the mushrooming penetration mode differs from that in its original state (Fig. 18). The bcc phase turned into dendrites with particular morphologies compared with the original columnar dendrite. Besides, the dendrites were distributed in a cross shape and the proportion of the bcc phase decreased sharply. Macro-kinetics (thermodynamics) plays a leading role in dendrite growth. The effect of thermodynamic and kinetic factors on dendrite growth is unified by undercooling. At higher undercooling, the growth rate of dendrite increases. The penetration process is accompanied by high pressure and temperature. The undercooling caused by temperature and shock pressure
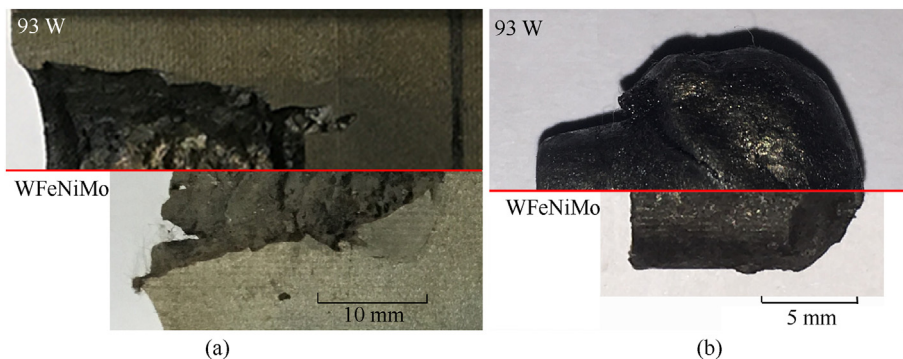

(a)

(b)

Fig. 9. Comparison between WHA and HEA (a) Penetration channel; (b) Residual projectile.
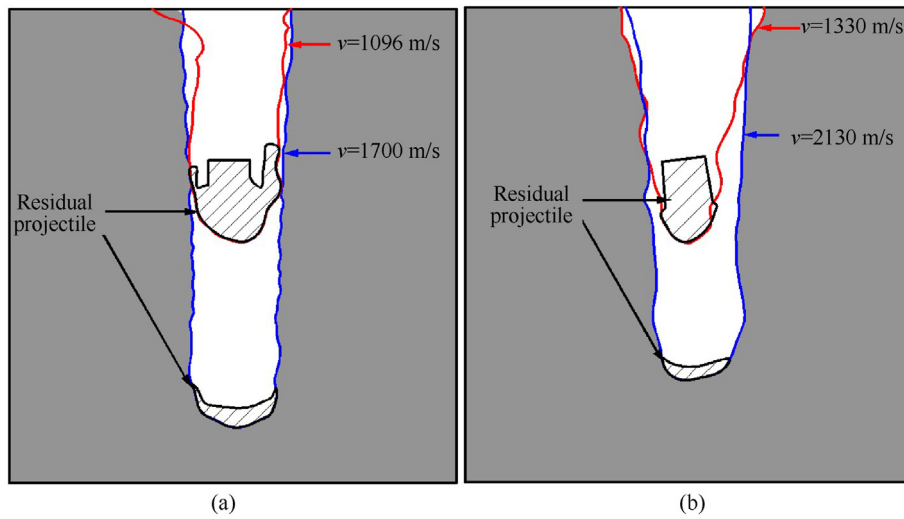
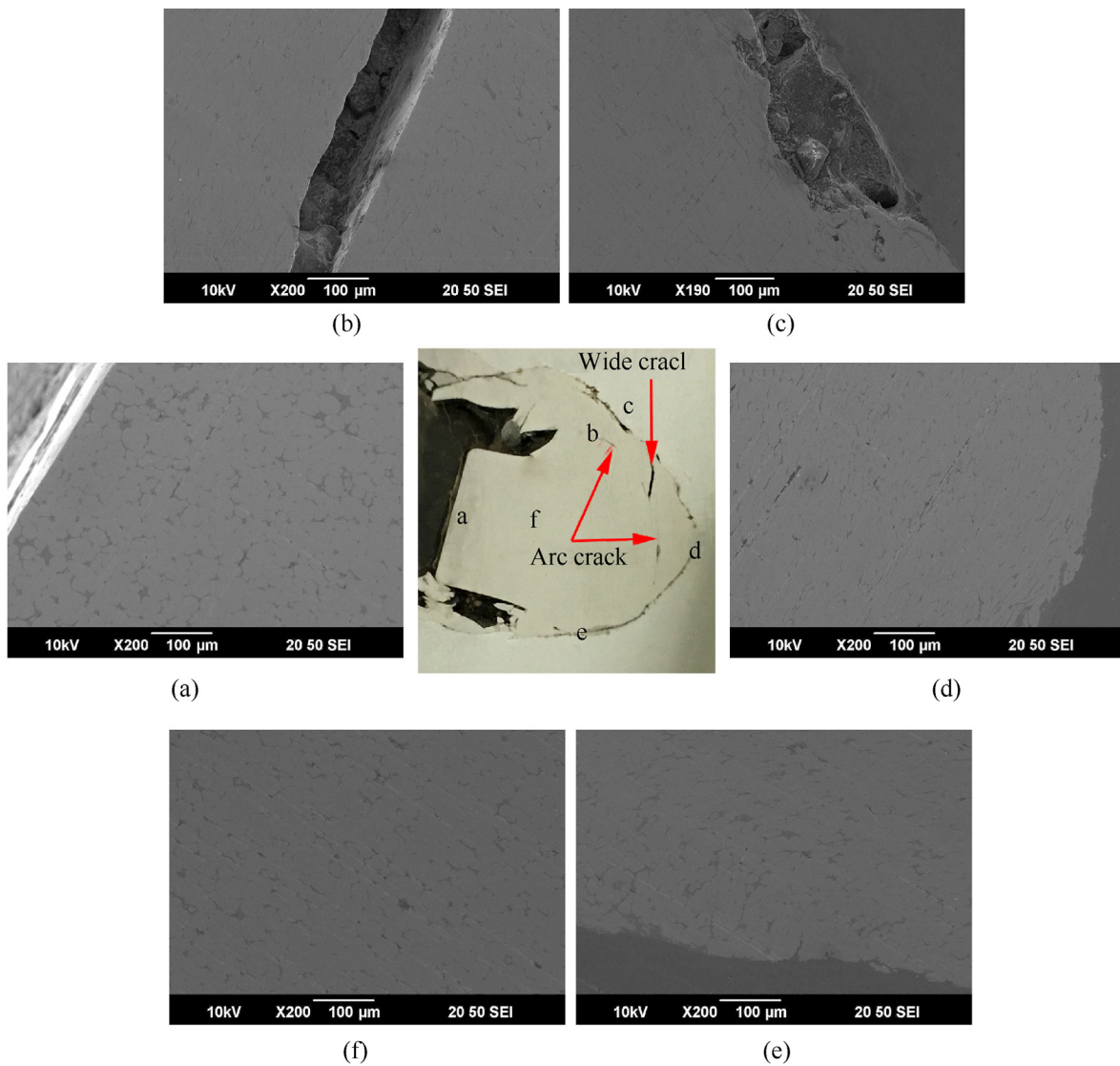**Fig. 10.** Penetration channel and residual projectile (a) WHA; (b) HEA.

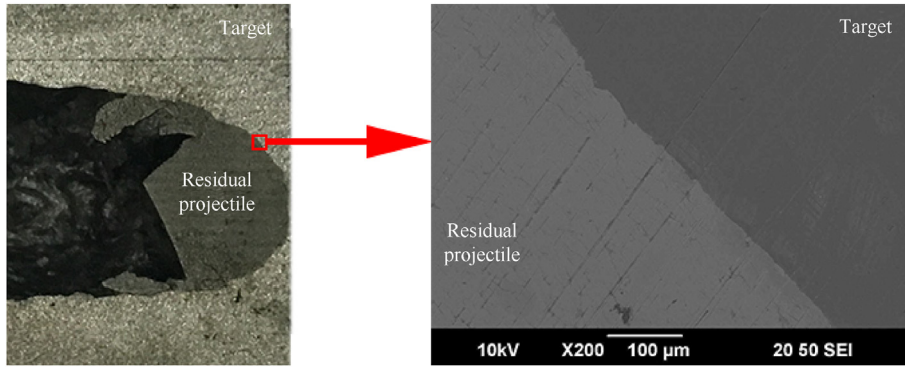**Fig. 11.** Metallography of WHA residual projectile (v = 1096 m/s).

Fig. 12. Metallography of WHA residual projectile ($v = 1583$ m/s).
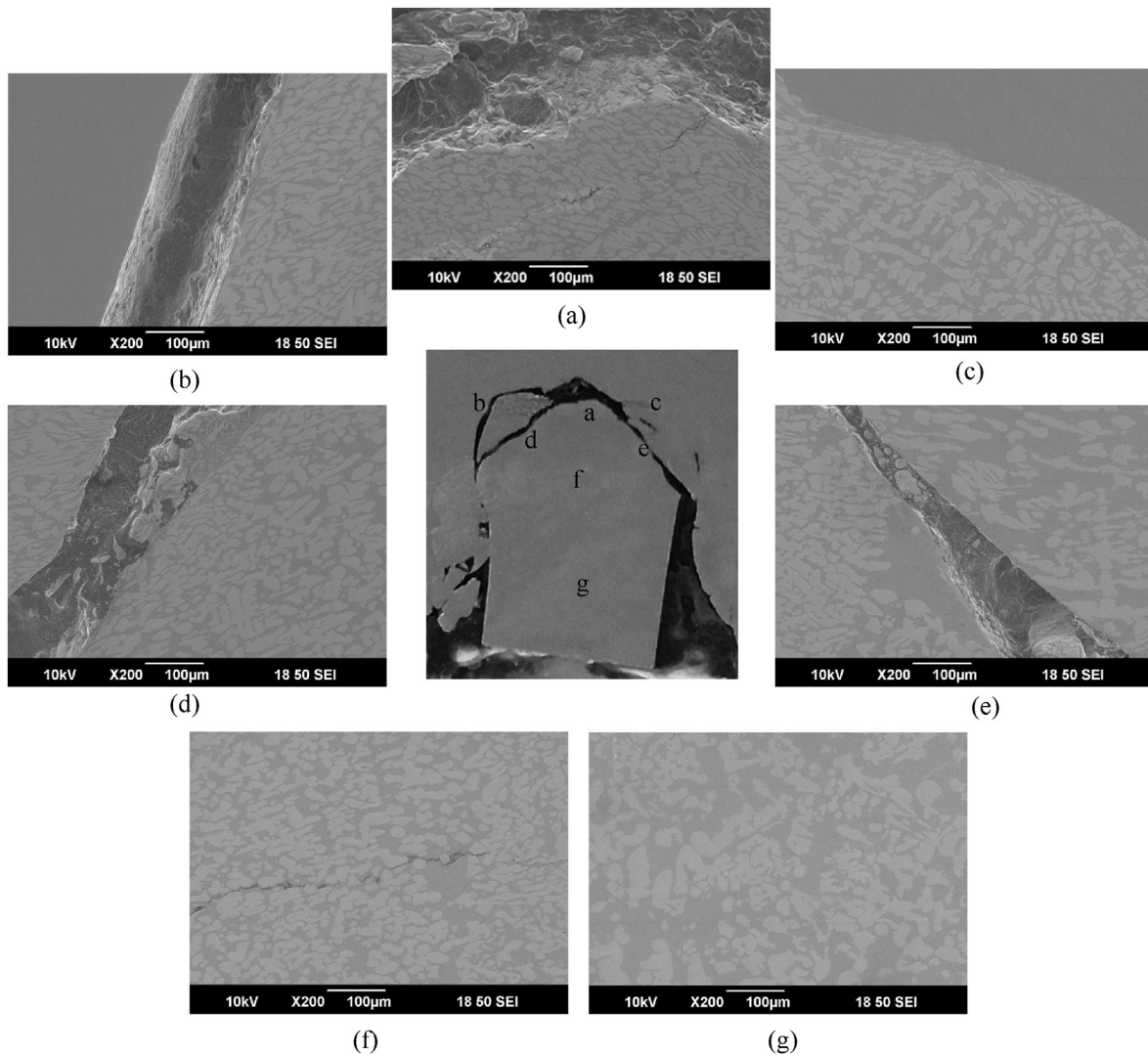

Fig. 13. Metallography of HEA residual projectile in the self-sharpening penetration mode($v = 1330$ m/s).

in the self-sharpening penetration mode cannot make the phase change. The projectile in the mushrooming penetration mode suffers higher temperature and shock pressure which caused the higher undercooling and the growth of dendrite.

In Fig. 19(a), the shear band was developed in the bcc phase, and the bcc phase deformed violently in both sides of the crack.

Similarly, the same situation is shown in Fig. 19(b), where the crack was developed in the shear band. To sum up, the multi-phase flow affects the HEA microscopic morphology and contributes to different mechanical properties. Furthermore, the evolution of microstructure will affect the penetration behavior ultimately.
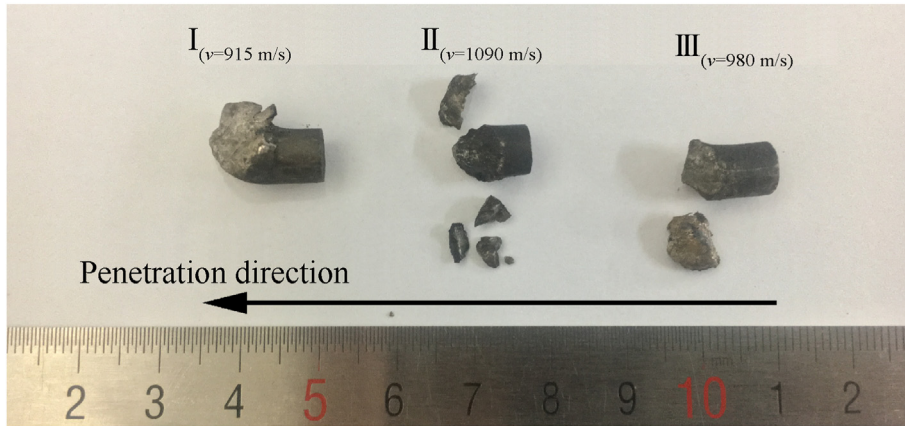
In conclusion, the self-sharpening and mushrooming

Fig. 14. Three penetration stages in the self-sharpening penetration mode (I: Shear band evolution; II: Crack propagation; III: Material separation).
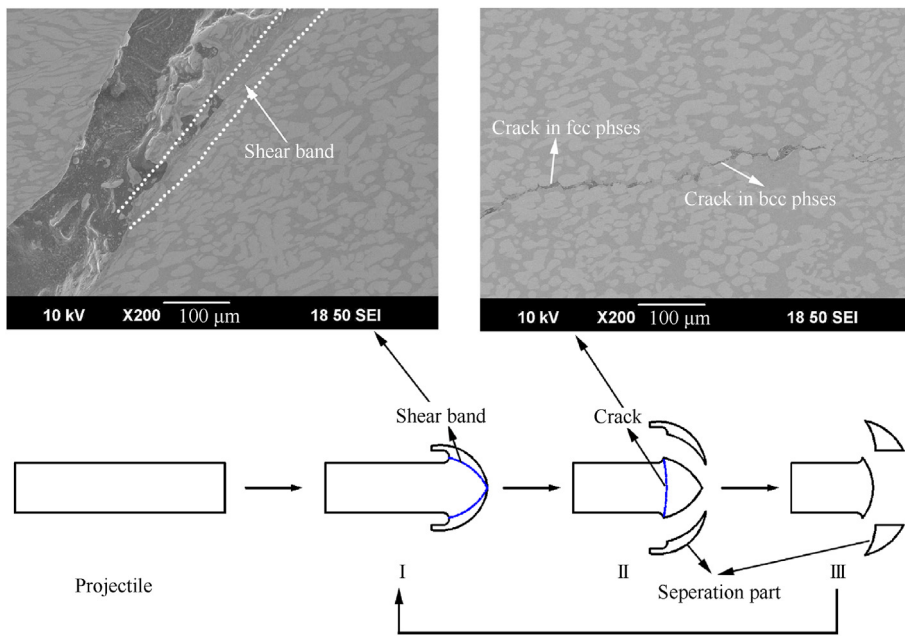

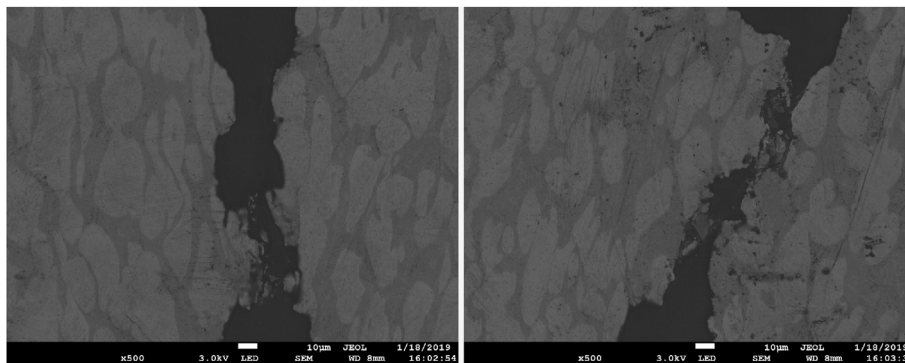**Fig. 15.** Deformation behavior evolution of the HEA projectile in three penetration stages.

Fig. 16. Cracks in the HEA projectile nose.

penetration modes differs in microstructure. The bcc phase of the HEA is disordered dendrites in the original state. When the HEA projectile enters the self-sharpening penetration mode, the phases are compressed and shear bands and cracks are developed in the fcc phases. When the projectile enters the mushrooming penetration mode, the bcc phase changes from disordered dendrites to
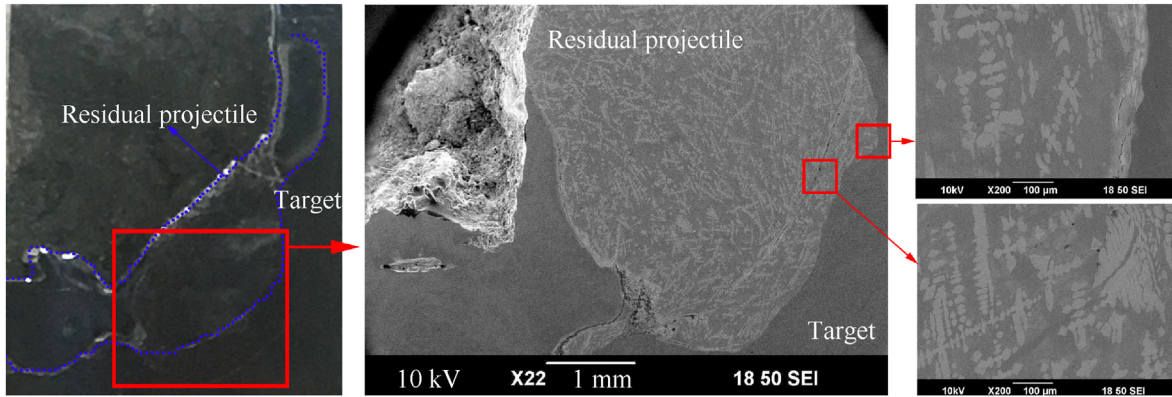
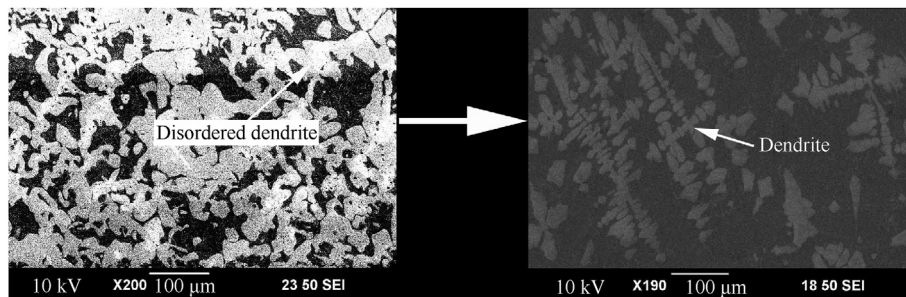**Fig. 17.** Metallography of HEA residual projectile in the mushrooming penetration mode (v = 1999 m/s).

Fig. 18. Comparison between disordered dendrites and dendrites of bcc phase.
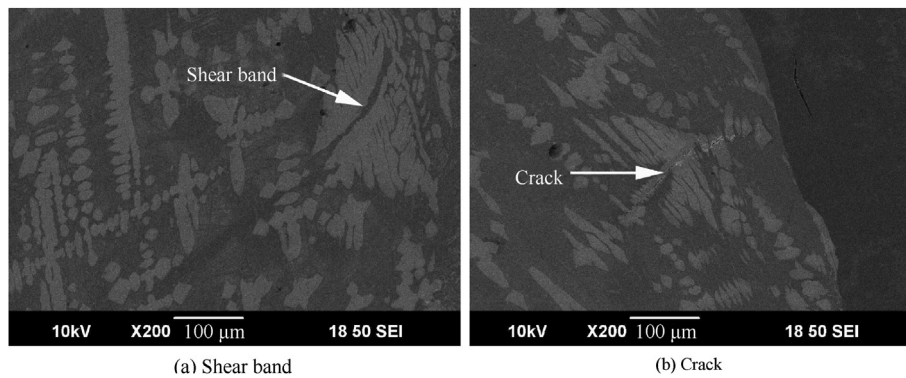

(a) Shear band

(b) Crack

Fig. 19. Shear band and crack developed in the dendrite.

dendrites with cross distribution. The shear bands and cracks are developed in the bcc phases, which are different from those in the self-sharpening penetration mode.

5. Summary and conclusions

In this paper, experiments of WFeNiMo HEA and WHA projectiles penetrating into the steel targets at impact velocities of 1100−1700 m/s for WHA and 1500−2200 m/s for HEA were carried out. Penetration behaviors of the two materials were analyzed with wide range of impact velocities. The transition of the HEA projectiles in the penetration was also validated. The residual projectiles were analyzed on both macro and micro scales. The shear band evolution in the self-sharpening penetration mode also differs from that in the mushrooming penetration mode. Based on the micro-structural characteristics of the HEA, the mechanism of

penetration mode transition was investigated. The main conclusions are as follows:

(1) As the impact velocity increases, the penetration mode of the WFeNiMo HEA projectile changes from self-sharpening to mushrooming penetration mode. The impact velocity of the transition is between 1330 m/s to 1531 m/s.

(2) The multi-phase interaction of HEA causes the inhomogeneous stress distribution in the nose of projectile and further leads to the three penetration stages in the self-sharpening penetration mode. A subtle crack causes the separation between the nose and the cylindrical part, and also has an effect on the material to be separated from the nose, which promotes the process of self-sharpening for the WFeNiMo HEA.

(3) The bcc phase changes from the disordered dendrite in the self-sharpening penetration mode to the dendrite with cross

distribution in the mushrooming penetration mode. The crack is developed mainly in the fcc phase in the self-sharpening penetration mode of the WFeNiMo HEA, while in the mushrooming penetration mode, it is developed in the bcc phase.

Declaration of competing interest

The authors declare that they have no known competing financial interests or personal relationships that could have appeared to influence the work reported in this paper.

Acknowledgement

References

[1] Wang F, Balbus GH, Xu S, et al. Multiplicity of dislocation pathways in a refractory multiprincipal element alloy. Science 2020;370(6512):95−101.

[2] George EP, Curtin W, Tasan CC. High entropy alloys: a focused review of mechanical properties and deformation mechanisms. Acta Mater 2020;188:435−74.

[3] Ding Q, Zhang Y, Chen X, et al. Tuning element distribution, structure and properties by composition in high-entropy alloys. Nature 2019;574(7777):223−7.

[4] Zhang W, Liaw PK, Zhang Y. Science and technology in high-entropy alloys. Science China Materials 2018;61(1):2−22.

[5] Miracle DB, Senkov ON. A critical review of high entropy alloys and related concepts. Acta Mater 2017;122:448−511.

[6] Tsai M-H, Yeh J-W. High-entropy alloys: a critical review. Materials Research Letters 2014;2(3):107−23.

[7] Zhang Y, Zuo TT, Tang Z, et al. Microstructures and properties of high-entropy alloys. Prog Mater Sci 2014;61(apr):1−93.

[8] Martin M, Shen T, Thadhani N. Instrumented anvil-on-rod impact experiments for validating constitutive strength model for simulating transient dynamic deformation response of metals. Materials Science and Engineering: A 2008;494(1−2):416−24.

[9] Conner R, Dandliker R, Scruggs V, et al. Dynamic deformation behavior of tungsten-fiber/metallic−glass matrix composites. Int J Impact Eng 2000;24(5):435−44.

[10] Choi-Yim H, Conner RD, Szuecs F, et al. Quasistatic and dynamic deformation of tungsten reinforced $Zr_{57}Nb_5Al_{10}Cu_{15.4}Ni_{12.6}$ bulk metallic glass matrix composites. Scripta Mater 2001;45(9):1039−45.

[11] Chen X, Wei L, Li J. Experimental research on the long rod penetration of tungsten-fiber/Zr-based metallic glass matrix composite into Q235 steel target. Int J Impact Eng 2015;79:102−16.

[12] Li J, Chen X, Huang F. FEM analysis on the "self-sharpening" behavior of tungsten fiber/metallic glass matrix composite long rod. Int J Impact Eng 2015;86:67−83.

[13] Li J, Chen X, Huang F. FEM analysis on the deformation and failure of fiber reinforced metallic glass matrix composite. Materials Science and Engineering: A 2016;652:145−66.

[14] Jiao WJ, Chen XW. Review on long-rod penetration at hypervelocity. Advances in mechanics 2019;49(1):312−91.

[15] Tate A. A theory for the deceleration of long rods after impact. J Mech Phys Solid 1967;15(6):387−99.

[16] Tate A. Further results in the theory of long rod penetration. J Mech Phys Solid 1969;17(3):141−50.

[17] Alekseevskii VP. Penetration of a rod into a target at high velocity 1966;2(2):63−6.

[18] Anderson CE. Analytical models for penetration mechanics: a Review. Int J Impact Eng 2017;108(oct):3−26.

[19] Rosenberg Z, Marmor E, Mayseless M. On the hydrodynamic theory of long-rod penetration. Int J Impact Eng 1990;10(1−4):483−6.

[20] Sun GC, Wu JY, Zhao GZ. A simplified model of the penetration of the long-rod penetrator against the plates with semi-infinite thickness at normal angle. Acta Armamentarii 1981;41−8.

[21] Zhang LS, Huang FL. Model for long-rod penetration into semi-infinite targets. J Beijing Inst Technol (Soc Sci Ed) 2004;13(3):285−9.

[22] Anderson CE, Littlefield DL, Walker JD. Long-rod penetration, target resistance, and hypervelocity impact. Int J Impact Eng 1993;14(1−4):1−12.

[23] Kong X, Wu H, Fang Q, et al. Projectile penetration into mortar targets with a broad range of striking velocities: test and analyses. Int J Impact Eng 2017;106:18−29.

[24] Rosenberg Z, Dekel E. The penetration of rigid long rods - revisited. Int J Impact Eng 2009;36(4):551−64.

[25] Anderson CE, Walker JD, Hauver GE. Target resistance for long-rod penetration into semi-infinite targets. Nucl Eng Des 1992;138(1):93−104.

[26] Rosenberg Z, Dekel E. The relation between the penetration capability of long rods and their length to diameter ratio. Int J Impact Eng 1994;15(2):125−9.

[27] Rosenberg Z, Malka-Markovitz A, Kositski R. Inferring the ballistic resistance of thick targets from static deep indentation tests. International Journal of Protective Structures 2018;9(3):347−61.

[28] Stepanov N, Shaysultanov D, Salishchev G, et al. Effect of V content on microstructure and mechanical properties of the CoCrFeMnNiVx high entropy alloys. J Alloys Compd 2015;628:170−85.

[29] Fang S, Chen W, Fu Z. Microstructure and mechanical properties of twinned $Al_{0.5}CrFeNiCo_{0.3}C_{0.2}$ high entropy alloy processed by mechanical alloying and spark plasma sintering. Mater Des 2014;54:973−9.

[30] Liu S, Gao M, Liaw P, et al. Microstructures and mechanical properties of $Al_xCrFeNiTi_{0.25}$ alloys. J Alloys Compd 2015;619:610−5.

[31] Ji W, Wang W, Wang H, et al. Alloying behavior and novel properties of CoCrFeNiMn high-entropy alloy fabricated by mechanical alloying and spark plasma sintering. Intermetallics 2015;56:24−7.

[32] Kumar N, Ying Q, Nie X, et al. High strain-rate compressive deformation behavior of the $Al_{0.1}CrFeCoNi$ high entropy alloy. Mater Des 2015;86:598−602.

[33] Ma S, Jiao Z, Qiao J, et al. Strain rate effects on the dynamic mechanical properties of the $AlCrCuFeNi_2$ high-entropy alloy. Materials Science and Engineering: A 2016;649:35−8.

[34] Wang B, Fu A, Huang X, et al. Mechanical properties and microstructure of the CoCrFeMnNi high entropy alloy under high strain rate compression. J Mater Eng Perform 2016;25(7):2985−92.

[35] Li Z, Zhao S, Diao H, et al. High-velocity deformation of $Al_{0.3}CoCrFeNi$ high-entropy alloy: remarkable resistance to shear failure. Sci Rep 2017;7:42742.

[36] Jiang Z, He J, Wang H, et al. Shock compression response of high entropy alloys. Materials Research Letters 2016;4(4):226−32.

[37] Zhang Z, Zhang H, Tang Y, et al. Microstructure, mechanical properties and energetic characteristics of a novel high-entropy alloy $HfZrTiTa_{0.53}$. Mater Des 2017;133:435−43.

[38] Liu XF, Tian ZL, Zhang XF, et al. "Self-sharpening" tungsten high-entropy alloy. Acta Mater 2020;186:257−66.

[39] Davitt RP. A comparison of the advantages and disadvantages of depleted uranium and tungsten alloy as penetrator materials. 1980.

[40] Magness LS. High strain rate deformation behaviors of kinetic energy penetrator materials during ballistic impact. Mech Mater 1994;17(2−3):147−54.

[41] Li Z, Tasan CC, Pradeep KG, et al. A TRIP-assisted dual-phase high-entropy alloy: grain size and phase fraction effects on deformation behavior. Acta Mater 2017;131:323−35.